



Can the Violent Merger of White Dwarfs Explain the Slowest Declining Type Ia Supernova SN 2011aa?

Anirban Dutta^{1,2}, G. C. Anupama¹, Nand Kumar Chakradhari³, and D. K. Sahu¹

¹ Indian Institute of Astrophysics, II Block, Koramangala, Bangalore 560034, India; anirban.dutta@iiap.res.in, anirbaniamdutta@gmail.com

² Pondicherry University, R.V. Nagar, Kalapet, 605014, Puducherry, India

³ School of Studies in Physics & Astrophysics, Pt. Ravishankar Shukla University, Raipur 492010, India

Received 2022 June 29; revised 2022 September 1; accepted 2022 September 1; published 2022 October 21

Abstract

We present optical observations and Monte Carlo radiative transfer modeling of the Type Ia supernova (SN Ia) SN 2011aa. With a $\Delta m_{15}(B)$ of 0.59 ± 0.07 mag and a peak magnitude M_B of -19.30 ± 0.27 mag, SN 2011aa has the slowest decline rate among SNe Ia. The secondary maximum in the *I* band is absent or as equally bright as the primary maximum. The velocity of C II is lower than the velocity of Si II. This indicates either the presence of C at lower velocities than Si or a line-of-sight effect. Application of Arnett's radiation diffusion model to the bolometric light curve indicates a massive ejecta M_{ej} 1.8–2.6 M_{\odot} . The slow decline rate and large ejecta mass, with a normal peak magnitude, are well explained by a double degenerate, violent merger explosion model. The synthetic spectra and light curves generated with SEDONA considering a violent merger density profile match the observations.

Unified Astronomy Thesaurus concepts: [Supernovae \(1668\)](#)

Supporting material: data behind figures

1. Introduction

Type Ia supernovae (SNe Ia) result from thermonuclear explosions of white dwarf (WD) stars in binary systems (Hoyle & Fowler 1960; Jha et al. 2019). The rate of decline in normal type Ia SNe ($0.85 < \Delta m_{15}(B) < 1.70$ mag) is correlated with the absolute magnitude in the *B* band (Phillips 1993). The radioactive decay of ^{56}Ni to ^{56}Co and finally to ^{56}Fe supplies the energy during the maximum of the light curve and its subsequent evolution (Pankey 1962; Colgate & McKee 1969; Branch & Wheeler 2017). In addition, the efficiency with which gamma rays and positrons from the decay of ^{56}Ni are trapped in the ejecta also plays an important role in the evolution of the light curve (Cappellaro et al. 1997). The luminosity also increases with more ^{56}Ni produced in the explosion. This increased luminosity causes the ejecta to have a higher temperature. The opacity increases with temperature, and the diffusion timescales for the photons increases. This results in slower decline and broader light curves (Hoeftlich et al. 1996). Hence, the decline rate versus absolute magnitude relation can also be interpreted as an opacity effect (Baron et al. 2012). While a majority of SNe Ia follow the luminosity decline rate relation, it is important to note that a good fraction of SN events that are of thermonuclear origin do not follow this relation (Maeda & Terada 2016; Taubenberger 2017). The overluminous super-Chandrasekhar SNe Ia (Howell et al. 2006; Ashall et al. 2021) lie at the extreme end of the $\Delta m_{15}(B)$ – M_B relation. They are slowly declining objects. The SNe Iax (SN 2002cx-like) are a peculiar class of thermonuclear explosions having low luminosity and low kinetic energy as compared to SNe Ia (Li et al. 2003; Dutta et al. 2022).

In the proposed progenitor scenario for SNe Ia, the exploding WD can have a nondegenerate star (single degenerate (SD)) or another WD (double degenerate (DD)) as its binary companion. In

the SD scenario, the WD can accrete matter from a red-giant (Munari & Renzini 1992), sub-giant/main-sequence (van den Heuvel et al. 1992), or a He star (Liu et al. 2010). In the DD case, a violent merger of two similar-mass WDs ($\sim 0.9 M_{\odot}$) has been shown to give rise to a subluminous type Ia SN explosion (Pakmor et al. 2010). However, more massive primary WDs, due to their higher densities will produce more ^{56}Ni and Fe group elements (IGEs) and give rise to brighter SNe Ia (Pakmor et al. 2012).

Using preexplosion Hubble Space Telescope images Li et al. (2011) has ruled out He stars or luminous red giants as the companion of SN 2011fe. But a main-sequence star (Nugent et al. 2011) or another WD as a companion cannot be ruled out. Observations of early UV emission in a thermonuclear SN iPTF14atg (Cao et al. 2015) hinted toward collision of ejecta material with its companion, supporting an SD scenario. The excess flux can also be explained by ^{56}Ni in the outer layers (Magee & Maguire 2020). Some circumstellar mass can be formed from ejection of mass in tidal tails before the merger of two WDs. The interaction of the SN ejecta with the tidal tail ejecta produces signatures in X-ray/UV/optical (Raskin & Kasen 2013). The persistent presence of hydrogen in the spectra of PTF11kx can be understood in terms of ejecta interacting with circumstellar mass indicating a nondegenerate companion (Dilday et al. 2012; Silverman et al. 2013; Graham et al. 2017). The detection of [O I] $\lambda\lambda$ 6300, 6364 in the nebular spectra of SN 2010lp indicates that oxygen is present close to the center, which is predicted by a violent merger scenario (Taubenberger et al. 2013; Kromer et al. 2013). So, the very question of single/double degenerate progenitor still persists. The observed diversity in the explosions along with different models proposed to explain the diversity makes it important to study these systems.

In this Letter, we present optical observations and radiative transfer modeling with SEDONA of the spectra and light curves of a peculiar SN Ia, SN 2011aa. SN 2011aa was discovered on 2011 February 6.3 in the galaxy UGC 3906 (PGC 021381) at α (J2000) = $07^{\text{h}}36^{\text{m}}42^{\text{s}}.63$ and δ (J2000) = $+74^{\circ}26'34''.80$ (Puckett et al. 2011). There is another nearby galaxy PGC 021386

with a similar radial velocity to PGC 021381, making it a galaxy pair, with the SN located in between the two galaxies. Gurugubelli et al. (2011) classified it as an SN Ia a few days before maximum light. The Swift-UV observations of SN 2011aa were presented in Brown et al. (2014). Friedman et al. (2015) have cataloged the JHK_s photometry of SN 2011aa.

We organize the paper as follows: Section 2 briefly discusses the observations and data reduction. The *UVOIR* bolometric light curve and spectral evolution are analyzed in Section 3. We discuss possible explosion models in Section 4. Section 5 contains the Monte Carlo radiative transfer simulations and comparison of the synthetic spectra and light curves with the observed ones. Finally, we note the important features of SN 2011aa in Section 6.

2. Data

SN 2011aa was observed in imaging and spectroscopic mode with the 2 m Himalayan Chandra Telescope⁴ (HCT) of the Indian Astronomical Observatory (IAO), Hanle, India. Photometric monitoring of SN 2011aa began on 2011 February 8 (JD 2455601.33) and continued until 2011 June 27 (JD 2455740.13). Spectroscopic observation of SN 2011aa was carried out during 2011 February 8 (JD 2455601.36) to 2011 April 29 (JD 2455681.18).

The images were obtained in Bessell UBVR filters and the spectra were obtained using grisms Gr 7 (3500–7800 Å) and Gr 8 (5200–9100 Å) with the Himalayan Faint Object Spectrograph Camera (HFOSC), mounted on the HCT. Data are reduced in the same manner as described in Dutta et al. (2021). Magnitudes are estimated using point-spread function fitting photometry and calibrated with respect to secondary standards in the field.

The UltraViolet Optical Telescope (UVOT) on board the Swift satellite observed SN 2011aa in three broadband optical filters u , b , and v and three UV filters $uvw2$, $uvm2$, and $uvw1$, during ~ -8 days to $\sim +45$ days with respect to the B -band maximum. The Swift-UVOT data were downloaded from the Swift archive and reduced using various modules in High Energy Astrophysics Software following the methods of Poole et al. (2008), Brown et al. (2009), and Chakradhari et al. (2014).

3. Light Curves and Spectra

3.1. Light Curve Analysis

The light curves of SN 2011aa in Bessell UBVR and Swift-UVOT $uvw2$, $uvm2$, $uvw1$, u , b , and v bands are plotted in Figure 1. The date of maximum and the maximum magnitude are estimated by performing Gaussian process regression (Rasmussen & Williams 2006) with Matern kernel on the light curves, using the `Gaussian_process` package in `scikit-learn` (Pedregosa et al. 2011). Gaussian processes are a supervised machine-learning method designed to solve problems of regression. The errors are the standard deviation of 1000 such iterations. The peak in the B band occurred at JD 2455611.65 \pm 1.05 with a magnitude of 14.72 \pm 0.01 mag. The $\Delta m_{15}(B)$ is estimated to be 0.59 \pm 0.07, making it the slowest declining SN Ia. The peak in the U band occurred at JD 2455611.35 \pm 0.53 (−0.3 day) and that in the V , R , and I bands occurred at JD 2455615.52 \pm 0.44 (+3.8 days), 2455616.10 \pm 0.44 (+4.5 days) and 2455618.72 \pm 0.46

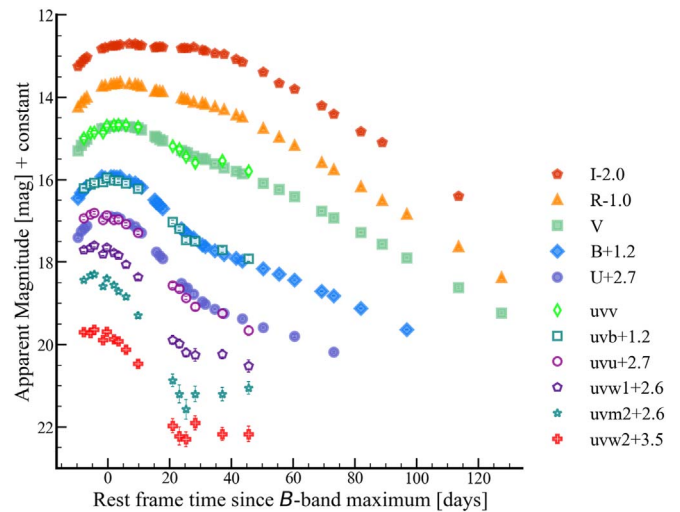


Figure 1. Optical UBVR and Swift-UVOT light curves of SN 2011aa. The horizontal axis represents rest-frame time since the B -band maximum ($(t-t_{\max})/(1+z)$). The magnitudes are given in the *Vega* system. The light curves have been vertically shifted by the amount indicated in the figure.

(The data used to create this figure are available.)

(+7.1 days). The I -band light curve does not show secondary peak, which is a characteristic of a normal SN Ia.

SN 2011aa exploded 20''4 east and 10''2 south of the center of UGC 3906 (Puckett et al. 2011). The radial velocity of UGC 3906 corrected for Local Group infall onto Virgo is 3995 \pm 20 km s^{−1} (Makarov et al. 2014). The calculated luminosity distance is 56.3 \pm 0.3 Mpc and the distance modulus 33.75 \pm 0.27 mag, assuming $H_0 = 70$ km s^{−1} Mpc^{−1}, $\Omega_M = 0.27$, and $\Omega_\Lambda = 0.73$. The reddening is $E(B - V) = 0.0237 \pm 0.0006$ due to the dust in the Milky Way (Schlafly & Finkbeiner 2011). However, in the near-maximum spectrum of SN 2011aa we observe NaID ($\lambda 5890$) absorption with a pseudo-equivalent width (pEW) of 0.41 \pm 0.02 Å due to interstellar medium in the Milky Way. Using the empirical relation $E(B - V) = 0.16 \times \text{pEW}(\text{NaID})$ (Turatto et al. 2003), we get $E(B - V) = 0.065 \pm 0.003$ mag. We do not detect any NaID at the redshift of the host galaxy, consistent with the location of SN 2011aa. The extinction in each band is estimated using Cardelli et al. (1989) with $R_V = 3.1$. The absolute magnitude in the B band is -19.30 ± 0.27 mag, which is similar to normal SNe Ia.

3.2. Nickel Mass and Ejecta Mass

We obtain the *UVOIR* bolometric light curve using the Swift-UVOT, UBVR, and JHK_s band magnitudes. The UV contribution is 20% at -8.7 days and decreases to 3% at $+27$ days since the B -band maximum. For the first two epochs before -8.7 days we do not have UV magnitudes, so we add a 20% contribution to the optical. The NIR data coverage is from JD 2455616.17 to JD 2455657.19. The NIR contribution to the UV-optical luminosity is 10% at JD 2455616 (+4.4 days) and increases to 25% at JD 2455640 (+28.6 days). We assume a constant contribution of 10% from NIR before +4.4 days. The *UVOIR* spectral energy distribution has been integrated from 1600 to 24800 Å.

We fit the light curve with a modified radiation diffusion model (See Equation (9) of Chatzopoulos et al. 2012) up to 70 days since the B -band maximum to obtain the parameters t_{exp} —the epoch of

⁴ https://www.iap.res.in/?q=telescope_iao

explosion, M_{Ni} —the ^{56}Ni mass produced, t_{lc} —the light-curve timescale, and t_{γ} —the gamma-ray leaking timescale. It is assumed that the initial radius of the progenitor is negligible compared to the expansion of the ejecta. A more realistic picture of the ejecta includes nonconstant opacity and varying spatial distribution of the energy density (^{56}Ni mixing; Khatami & Kasen 2019; Kushnir & Katz 2019). We used the `emcee` package in `python` to find the posterior distribution and hence the upper and lower error limits. The details of the fitting procedure are described in Dutta et al. (2022).

The fit to the *UVOIR* bolometric light curve gives $t_{\text{exp}} = 245, 5591.62^{+1.01}_{-1.41}$, $M_{\text{Ni}} = 0.87^{+0.06}_{-0.06} M_{\odot}$, $t_{\text{lc}} = 16.82^{+1.68}_{-1.79}$ days, and $t_{\gamma} = 55.42^{+3.00}_{-3.02}$ days. The rise time in the *B* band from t_{exp} is $20.03^{+1.58}_{-1.48}$ days. Using a constant optical opacity $\kappa_{\text{opt}} = 0.1 \text{ cm}^2 \text{ g}^{-1}$ and an expansion velocity $v_{\text{exp}} = 12,000 \text{ km s}^{-1}$ derived from the near-maximum spectrum, we get $M_{\text{ej}} = 2.64^{+0.53}_{-0.56} M_{\odot}$ and a kinetic energy of explosion $E_{\text{kinetic}} = 2.26^{+0.45}_{-0.48} \times 10^{51} \text{ erg}$. For a constant optical opacity of $0.15 \text{ cm}^2 \text{ g}^{-1}$, we get $M_{\text{ej}} = 1.76^{+0.35}_{-0.37} M_{\odot}$ and a kinetic energy of explosion $E_{\text{kinetic}} = 1.51^{+0.30}_{-0.32} \times 10^{51} \text{ erg}$. The ^{56}Ni mass is within the range for normal SNe Ia, $0.09\text{--}0.87 M_{\odot}$ with $\Delta m_{15}(B)$ between 0.8 and 1.9 mag (Stritzinger et al. 2006). The estimated M_{ej} is higher than expected for a normal SN Ia from an M_{ch} WD explosion. In order to understand the explosion mechanism and progenitor, we explore explosion models that can produce the ejecta and ^{56}Ni mass as estimated by the analytical one-dimensional model (See Section 4).

3.3. Spectral Evolution

The spectral sequence of SN 2011aa is shown in Figure 2(a). The spectra at -10.2 days shows features due to Si II, Si III, Fe III, S II, C II, O I, and Ca II. SN 2011aa falls under the core-normal class of the Branch classification (Branch et al. 2006). C II $\lambda 6580$ and C II $\lambda 7234$ are seen in the spectra until 17 days since the *B*-band maximum (Figure 2(a)).

The ejecta velocity is measured by fitting a Gaussian function to the Si II $\lambda 6355$ absorption feature. The velocity is $\sim 14,000 \text{ km s}^{-1}$ at -10.2 days and decreases by 200 km s^{-1} each day to reach $12,200 \text{ km s}^{-1}$ around the maximum. After maximum, the velocity evolves more slowly reaching about $12,000 \text{ km s}^{-1}$ at 3.5 days postmaximum. The spectroscopic evolution is slow and forms a velocity plateau. This places SN 2011aa in the low velocity gradient group of the Benetti classification scheme (Benetti et al. 2005). The velocity of C II $\lambda 6580$ is $8980 \pm 200 \text{ km s}^{-1}$ at -10.2 days and decreases to 3600 km s^{-1} at $+10.4$ days. The velocity of C II $\lambda 7234$ is $6650 \pm 690 \text{ km s}^{-1}$ at -1.4 days and decreases to $3670 \pm 180 \text{ km s}^{-1}$ at $+10.4$ days. The detonation wave proceeds faster at higher densities and the unburned material like C should be present at a higher velocity, lower density layer as compared to Si. The presence of C at lower velocities than Si may indicate that the photosphere at that epoch moves with the velocity of C, while the Si layer is moving faster or has ejecta asymmetries/clumping (Parrent et al. 2011).

In Figures 2(b), (c), and (d) we compare the spectra of SN 2011aa with SN 1991T (Filippenko et al. 1992), SN 2001ay (Krisciunas et al. 2011), SN 2005cf (Wang et al. 2009a), SN 2006gz (Hicken et al. 2007), SN 2009dc (Taubenberger et al. 2011), and SN 2013cv (Cao et al. 2016) at various epochs of evolution. The spectroscopic evolution of SN 2011aa shows most differences with the comparison SNe in the early phase. It

is quite different from bright SN 1991T-like objects that show weak/no features due to intermediate mass elements in the premaximum spectra. A super-Chandra object like SN 2009dc ($M_{\text{B}} = -20.22$ mag with a $\Delta m_{15}(B) = 0.71$ mag) produces $1.8 M_{\odot}$ of ^{56}Ni mass and $2.8 M_{\odot}$ of ejecta. It shows a strong absorption feature of C II (6580 \AA) in its spectra (Taubenberger et al. 2011) and is part of the shallow silicon (SS) group (Branch et al. 2006). Another super-Chandra object SN 2006gz has velocity of $\sim 12,000 \text{ km s}^{-1}$ near maximum light and falls in the SS group. The velocity of C is more than Si in SN 2006gz. SN 2011aa does not show strong features due to Ca II as seen in normal SN 2005cf. SN 2013cv shows the transitional nature between super-Chandra and normal SNe. It has a lack of IGEs in the early phase spectra and a persistent presence of C after maximum.

Now we discuss two objects that show some similarity with SN 2011aa in their light-curve evolution. The peculiar SN 2001ay (Krisciunas et al. 2011) exhibits slow decline ($\Delta m_{15}(B) = 0.68$ mag) with $M_{\text{B}} = -19.19$ mag. The Si II $\lambda 6355$ line is broad and its velocity evolution after maximum is quite rapid ($\sim 200 \text{ km s}^{-1} \text{ d}^{-1}$), which makes it to fall under the high velocity gradient group. This has been explained in terms of pulsational delayed detonation in an M_{ch} WD (Baron et al. 2012). In the case of the peculiar ASASSN-15hy (Lu et al. 2021) with a $\Delta m_{15}(B) = 0.72$ mag and $M_{\text{B}} = -19.14$ mag, the slow decline has been explained in terms of a degenerate core exploding inside a nondegenerate envelope. A large core mass is required in this case for understanding the broad light curves. The progenitor in this case is the merger of a WD with the core of an asymptotic giant branch star. The observed spectral properties of ASASSN-15hy is more similar to SN 2009dc with low velocity near the maximum (8000 km s^{-1}) and falls in the SS group. SN 2011aa is quite different in terms of spectroscopic evolution from both these objects.

4. Explosion Models

In this section, we discuss various possible explosion models that may explain the observables of SN 2011aa.

4.1. Collision of White Dwarfs

Collision between two WDs can occur in dense stellar environments like the core of globular clusters. Raskin et al. (2009) calculated about 10–100 WD collisions per year at redshift ≤ 1 . They calculated the explosion parameters for the collision of two equal mass WDs ($0.6 M_{\odot}$) for different impact parameters. The ^{56}Ni mass is maximum ($\sim 0.4 M_{\odot}$) for a head-on collision and decreases with increasing impact parameter. This ^{56}Ni mass is not consistent with SN 2011aa. Collision of higher-mass WDs ($\sim 0.9 M_{\odot}$) with a low impact parameter can produce brighter events that broadly follow the Phillips relation (see Figure 3 of Rosswog et al. 2009) with some dependence on the viewing angle. Using similar and dissimilar masses of the colliding WDs Kushnir et al. (2013) showed that SN Ia explosions are produced with ^{56}Ni mass in the range of $0.1\text{--}1.0 M_{\odot}$. Both the work of Rosswog et al. (2009) and Kushnir et al. (2013) showed that the ejecta structure is stratified with C and O in the outer layers, intermediate mass elements (IMEs) in the inner layers, and IGEs in the innermost layers caused as a result of detonation.

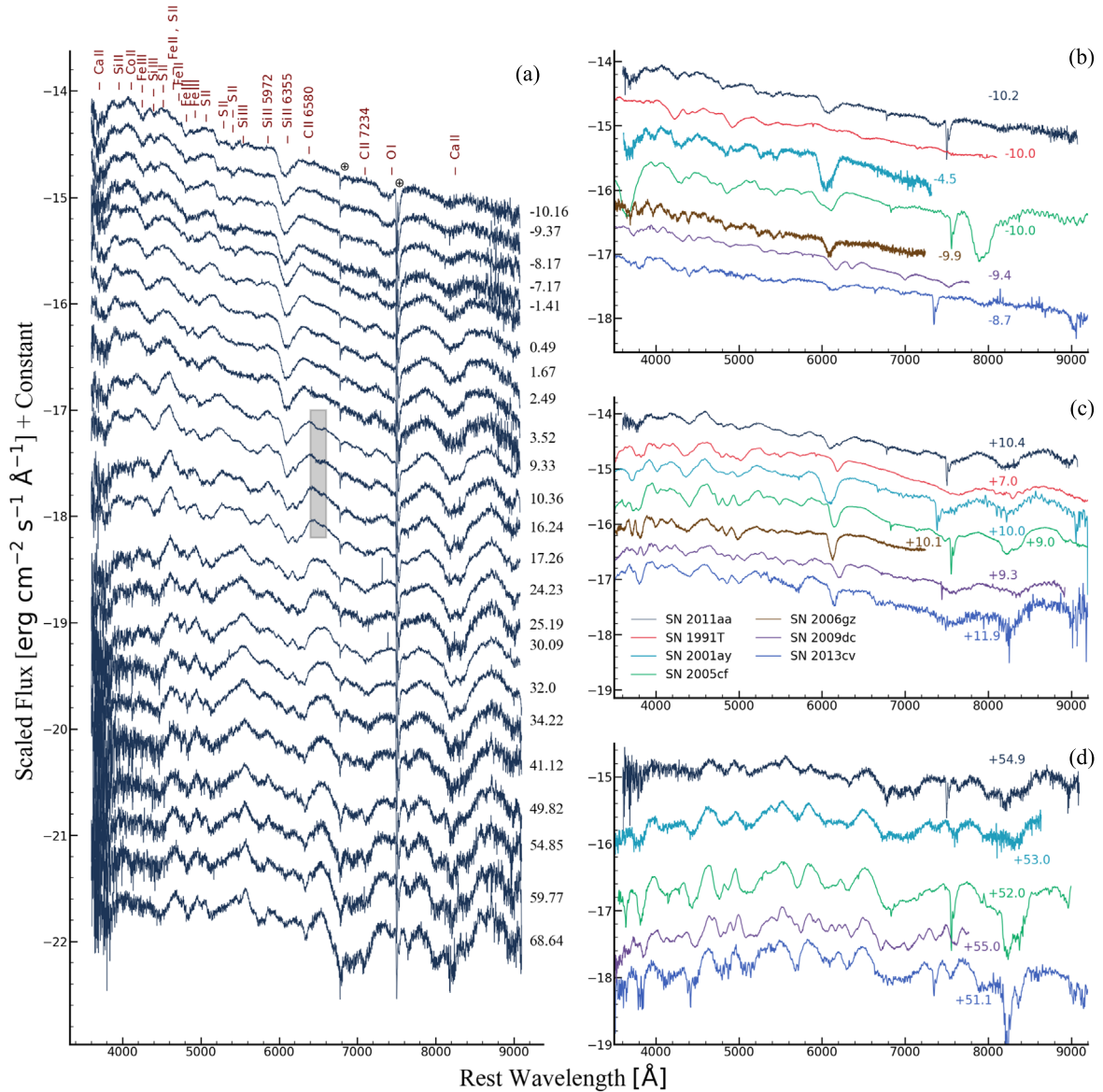


Figure 2. Spectral evolution of SN 2011aa from -10.16 to $+68.6$ days in the rest frame since the B -band maximum. The important lines for the premaximum spectra are marked in panel (a). C II $\lambda 6580$ region is shaded between 3.5 and 17.3 days since the B -band maximum. The observed spectra are dereddened and redshift corrected. Also shown is the comparison of SN 2011aa with luminous SN 1991T, peculiar SN 2001ay and SN 2013cv, normal SN 2005cf, and super-Chandra SN 2006gz and SN 2009dc at the premaximum (b), near-maximum (c) and postmaximum (d) phase.

(The data used to create this figure are available.)

4.2. Rotating White Dwarfs

The maximum mass of a nonrotating, inert WD is $\sim 1.4 M_{\odot}$ (M_{ch}). Carbon–oxygen WDs having differential rotation can support mass exceeding the Chandrasekhar limit (Yoon & Langer 2005). If the rotating WD is having a nondegenerate companion, the maximum possible mass that the accreting WD can reach by accretion is $2 M_{\odot}$ (Langer et al. 2000). The efficiency of the angular momentum gain and the loss will decide the final SN Ia explosion. We discuss explosion models based on rapidly rotating C–O WDs under hydrostatic equilibrium.

Fink et al. (2018) constructed WDs within mass range of 1.6 – $2.0 M_{\odot}$ and angular momentum between 0.9 and $2.2 \times 10^{50} \text{ g cm}^2 \text{ s}^{-1}$. Different explosion models like prompt detonation, delayed detonation (DDT), and pure deflagration models were tested. The prompt detonation model produces

$1.44 M_{\odot}$ of ^{56}Ni . In this model, the IMEs produced is extremely low. In the delayed detonation models, an initial deflagration develops, which transitions to a detonation due to the Zel’dovich gradient mechanism (mixing of hot ash with cold fuel under gravity). The mass of ^{56}Ni varies between 1.06 and $1.45 M_{\odot}$ based on the WD mass. All the DDT models show asymmetric ejecta structure. The models are luminous with the peak B -band absolute magnitude around ~ -20 mag. Of particular interest is the model AWD1, in which $1.06 M_{\odot}$ of ^{56}Ni is produced. This value is close to the ^{56}Ni mass estimate of SN 2011aa. But the model spectra is bluer with high blueshift of the Si II line. The model produces huge amount of IGEs ($1.31 M_{\odot}$) inconsistent with the observed spectra of SN 2011aa. The ejecta structure is also highly stratified with much less unburned C/O in the outer layers due to detonation.

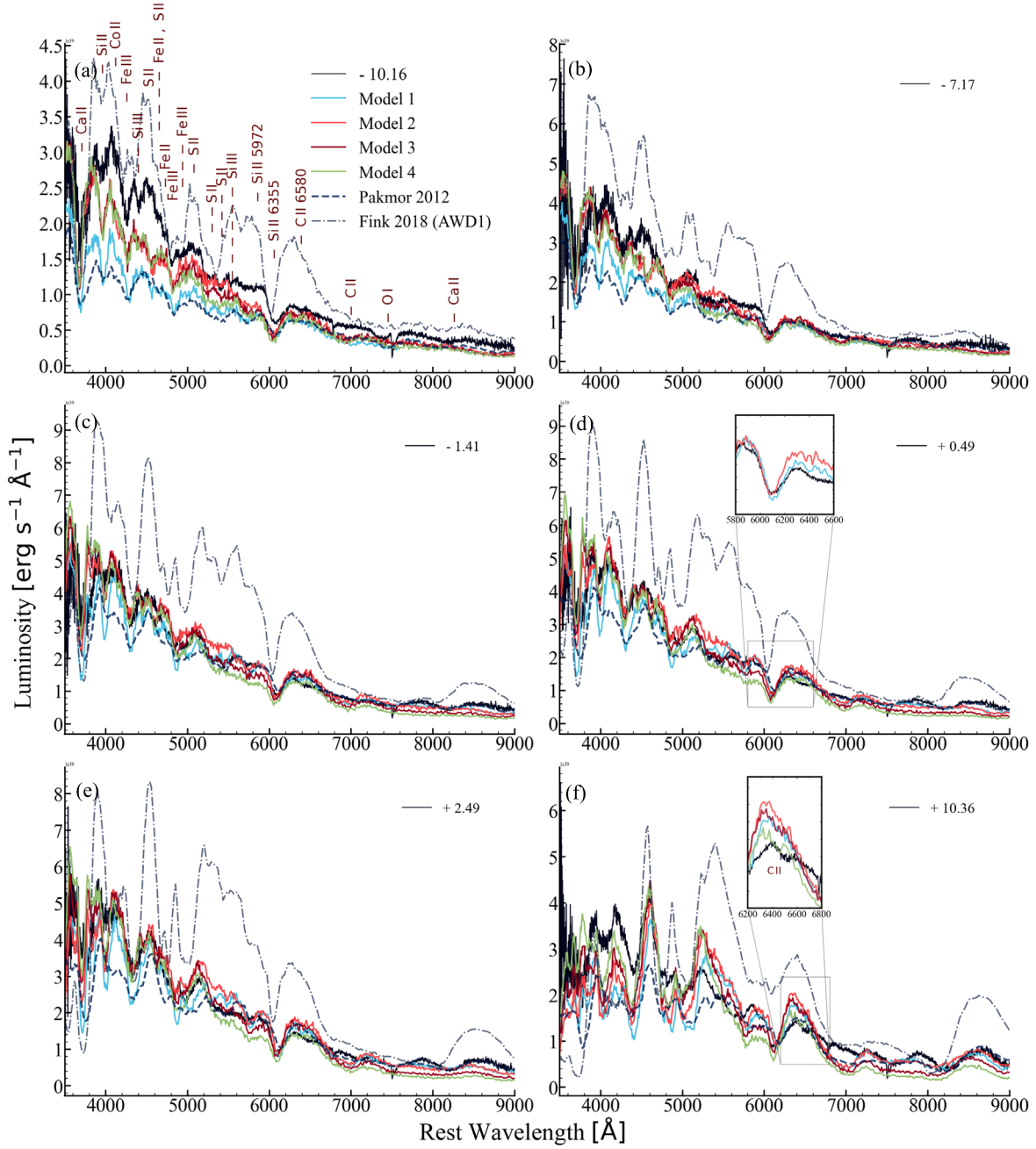


Figure 3. Spectral evolution of SN 2011aa from -10.16 to $+10.36$ days since rest-frame time in the B -band maximum. We show the model spectra calculated using SEDONA. Also shown are the angle averaged spectra of accreting WD model (AWD1) from Fink et al. (2018) and the violent merger model from Pakmor et al. (2012). These are taken from the HESMA database. The important lines in the early phase are marked in (a). The observed spectra are dereddened and redshift corrected.

We show the angle averaged spectra of AWD1 model (Fink et al. 2018) compared with SN 2011aa in Figure 3.

4.3. Violent Merger

Three-dimensional simulations of the violent merger of two C-O WDs of dissimilar masses (0.9 and $1.1 M_{\odot}$) can explain the normal type Ia explosions (Pakmor et al. 2012). The material from the secondary one is violently accreted onto the primary. The material is then compressed and heated up on the surface of the primary where carbon burning is ignited. At a density (ρ) $2 \times 10^6 \text{ g cm}^{-3}$ and at a temperature (T) greater than $2.5 \times 10^9 \text{ K}$ a detonation occurs. The detonation flame propagates through the final merged object and burns the material. The energy

released unbinds the object. The total ejected mass of this model ($\sim 1.95 M_{\odot}$) is comparable to that of SN 2011aa estimated using Arnett’s model. This model leads to an asymmetric explosion; hence, the observables have a line-of-sight dependence. In the B band the peak magnitude varies between -19.5 and -18.7 mag and the angle averaged magnitude is -19.0 mag. Similarly, the $\Delta m_{15(B)}$ varies between 0.5 and 1.4 mag with the mean value being 0.95 mag. The estimated values of the observables of SN 2011aa lie well within the range predicted by the violent merger model. The primary WD is burned and its ashes expand while the unburned and incompletely burned material (C, O, Ne, Mg) from the secondary WD resides near the center of the ejecta. Hence, the presence of C/O at lower velocities may be crucial in determining the explosion scenario. We show the angle averaged

spectra of violent merger model from Pakmor et al. (2012) in Figure 3. The spectra show some similarity in velocities and line strengths to SN 2011aa. This encourages us to use the violent merger model varying the abundances at different velocities to accurately model the line strengths and velocities and get estimates of mass of different elements synthesized. We used SEDONA with a violent merger density profile to model the observed spectra and light curve.

5. Modeling of the Spectra and Light Curves

We use the multidimensional Monte Carlo radiative transfer code SEDONA⁵ (Kasen et al. 2006) to simulate the spectral and light-curve evolution of SN 2011aa. The assumptions of the code are homologous expansion, Sobolev approximation, and local thermodynamic equilibrium (LTE). SEDONA takes into account the energy deposition from the radioactive decay of ^{56}Ni – ^{56}Co – ^{56}Fe . All the lines are treated in the expansion opacity formalism using the two-level atom approach. The parameter ϵ controls the probability of redistribution of radiation.

For all the models in this work, we use the spherical one-dimensional ejecta structure and the one-dimensional angle averaged density profile of the violent merger model (merger_2012_11+09; Pakmor et al. 2012). We consider 5×10^5 particles, 1000 frequency bins between 10^{14} Hz and 10^{16} Hz, and 100 logarithmically spaced time steps and start the simulation at 2 days since the explosion and evolve the models until 60 days. It is to be noted that for the purpose of resolving the most prominent features in the spectra, 5×10^5 particles is sufficient although increasing the number of particles will increase the resolution at the expense of computation time. We do not consider any best-fitting technique in this work.

Figure 3 shows the spectral evolution of SN 2011aa along with synthetic spectrum generated with SEDONA. We consider C, O, Ne, Na, Mg, Si, S, Ca, ^{54}Fe , ^{56}Ni , and ^{58}Ni in the models. We consider four models in this work based on the violent merger density profile. The integrated ejected mass is $1.95 M_{\odot}$ with a kinetic energy of 1.7×10^{51} erg for the models.

In the first model (Model 1), we use the abundance of the violent merger model (Pakmor et al. 2012), which produces $0.62 M_{\odot}$ of ^{56}Ni . In the model, C and O are present in the very inner layers ($<1000 \text{ km s}^{-1}$). This is due to the fact that the burning is not complete for the less-dense secondary WD and unburned elements dominate near the center after the ashes of the primary have expanded. ^{56}Ni is present up to $11,600 \text{ km s}^{-1}$. The layers between $10,000$ and $15,000 \text{ km s}^{-1}$ are dominated by Si, S, and Mg. The outer layers above $20,000 \text{ km s}^{-1}$ are mostly C and O.

The ^{56}Ni mass is lower than the mass estimated for SN 2011aa using Arnett model fit to the *UVOIR* light curve. In this model, the mass of unburned elements (C, O, and Ne) is $0.82 M_{\odot}$, intermediate mass elements (Mg, Si, S, Ca) is $0.47 M_{\odot}$, and IGEs (^{54}Fe , ^{56}Ni , and ^{58}Ni) is $0.67 M_{\odot}$. The model spectrum at -10.16 days since the *B*-band maximum is quite red and does not reproduce the observed continuum (Figure 3(a)). The Fe III, S II, and Mg II lines are very strong in the model (Figures 3(c) and (d)) indicating an overabundance of these elements. Near the maximum (+0.49 day) Si II $\lambda 6355$ and C II $\lambda 6580$ lines are reproduced well. In the spectrum taken +10.4 days after maximum, we see the C II $\lambda 6580$ absorption feature (see inset of

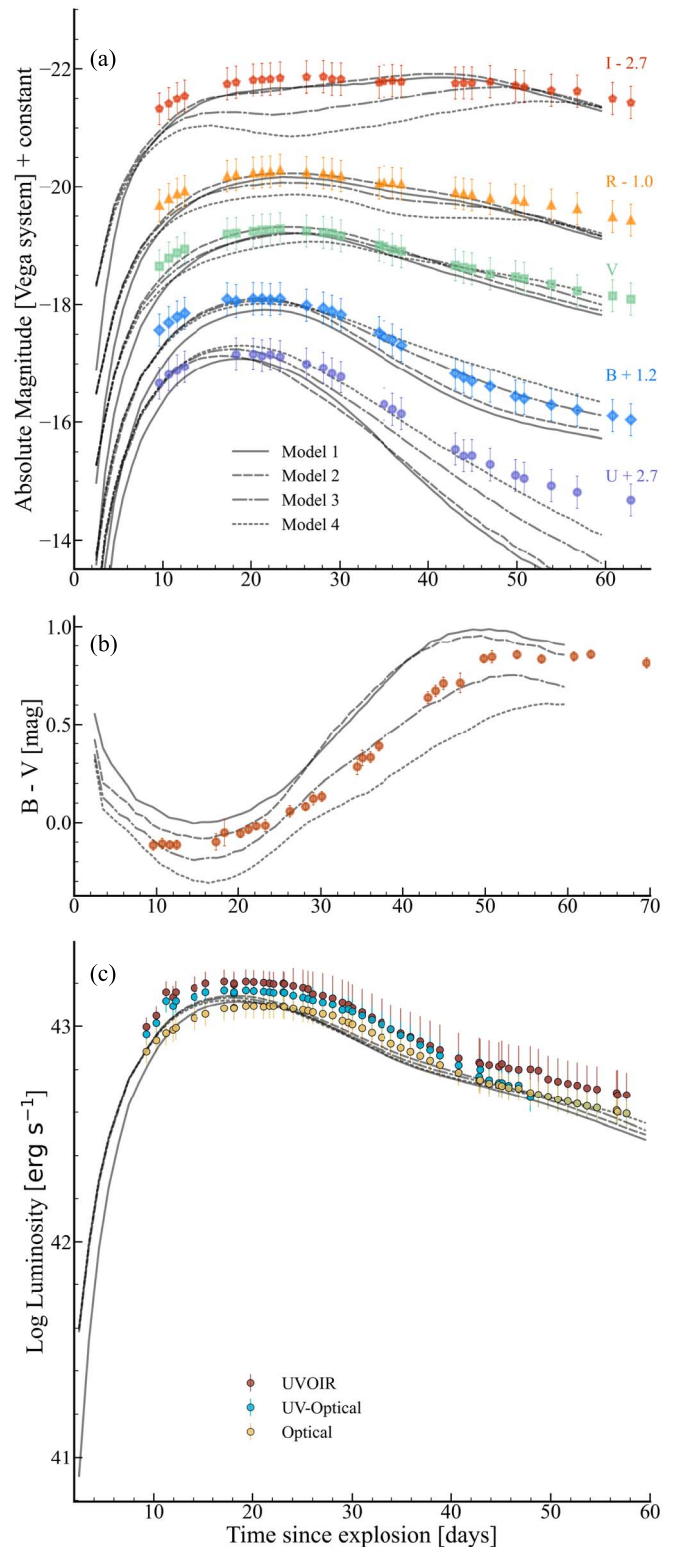


Figure 4. (a) The *U*-, *B*-, *V*-, *R*- and *I*-band light curves of SN 2011aa along with the synthetic light curves generated using SEDONA. From the model spectral energy distribution we calculate the light curves in the *AB* system and convert to *Vega* system using values given in Blanton & Roweis (2007). The horizontal axis is the time since the explosion (JD 2455591.62). (b) The *B* - *V* color evolution of SN 2011aa plotted along with the SEDONA models. (c) The optical, UV-optical, and *UVOIR* bolometric light curves is shown along with the models. The input SEDONA parameter and model files are provided as data behind the figure.

⁵ <https://github.com/dnkasen/pubsed>

Table 1
SEDONA Model Features

Model Name	Density ^a	Abundance	ϵ	$\Delta m_{15}(B)$ (mag)	M_B (mag)	^{56}Ni (M_\odot)
Model 1	violent merger	violent merger	1.0	0.96	−19.20	0.62
Model 2	violent merger	modified abundance + increased ^{56}Ni	1.0	0.96	−19.39	0.68
Model 3	violent merger	same as Model 2	0.5	0.77	−19.35	0.68
Model 4	violent merger	same as Model 2	0.3	0.59	−19.31	0.68

Note. The parameter and ejecta grid files for the four models generated with SEDONA are provided in the online journal.

^a One-dimensional density of the violent merger model.

Figure 3(f)). In normal SNe Ia, C is seen in the spectra during premaximum to maximum phases. However, in super-Chandrasekhar objects like SN 2009dc (Taubenberger et al. 2011), C can be seen in the postmaximum phases also. The detection of C in this phase indicates that C is present in the inner layers. This supports our argument of a violent merger scenario. At +10.4 days, the region below 5000 Å gets redder. This is mostly because of line blocking by IGEs.

To account for the ^{56}Ni mass estimate from the analytical light-curve model ($0.87 \pm 0.06 M_\odot$), we increased the mass fraction of ^{56}Ni at the expense of Mg and S between 10,000 and 16,000 km s^{−1} in the second model (Model 2). Between 8000 and 10,000 km s^{−1}, we decreased S and increased ^{56}Ni . We also reduced the mass fraction of ^{54}Fe between 8000 and 16,000 km s^{−1}. This allows to reproduce the line strengths of Fe III and S II in the models (Figures 3(c) and (d)). Near the maximum, the red wing of the Si II $\lambda 6355$ feature is stronger than the first model (see inset of Figure 3(d)). This is because of the higher ionization at lower velocities caused by an increased ^{56}Ni abundance. In this model, the ^{56}Ni mass is $0.68 M_\odot$. Further increasing the ^{56}Ni mass makes the red wing of Si II $\lambda 6355$ even stronger. Hence we do not consider increasing ^{56}Ni further.

The region below 5000 Å is redder than observed in this model also. For both the models, the redistribution probability ϵ is 1.0, which means absorption dominated treatment of the redistribution of radiation. Following a source function the absorption by a line is followed by a reemission in another frequency. This acts as fluorescence. We construct two more models varying the ϵ parameter. In these two models the abundances are same as the second model. In the third model (Model 3), with $\epsilon = 0.5$, meaning equal probability for scattering and absorption, we find slight improvement in reproducing the blueward flux at +10.4 days over the second model. In the fourth model (Model 4) $\epsilon = 0.3$, there is severe flux depression in the region around 5200–6000 Å and an increase in flux in the bluer region. This means in this model, the blue photons are scattered out of the ejecta more rather than being absorbed.

The light curves in each bandpass are obtained from the synthetic spectral energy distribution by convolving it with the HFOSC filter response. In Figure 4(a), we plot the observed light curves of SN 2011aa in *U*, *B*, *V*, *R* and *I* along with the model light curves from SEDONA simulation. Model 1 (solid curve in Figure 4(a)) underpredicts the magnitude in all bands. This is due to lower ^{56}Ni mass in the model ejecta. In Model 2 (dashed), we increase the ^{56}Ni mass and find that the peak in the *B* band is close (−19.39 mag) to the observed value (−19.30 ± 0.27 mag). But the decline rate is 0.96 mag, which is faster than the observed light curve (0.59 mag). In the model with $\epsilon = 0.5$ (dashed–dotted), the peak magnitude in the *B* band is −19.35 mag with a decline rate of 0.77 mag. In the fourth model $\epsilon = 0.3$ (dotted), the peak

magnitude is −19.31 mag with a decline rate of 0.59 mag in the *B* band. But the flux in the *I* band is severely underpredicted. The absent or equally bright secondary maximum is reproduced by our violent merger models (particularly Model 1 and Model 2). The extinction corrected *B* − *V* color is plotted and compared with the models in Figure 4(b). Model 1 is redder and Model 4 is bluer than the observed values throughout. Increasing ^{56}Ni makes Model 2 bluer than Model 1 around 10–20 days since explosion; however, this model becomes redder after 30 days. Model 3 predicts the color evolution better around 30–50 days. The optical, UV-optical, and *UVOIR* bolometric luminosity are plotted in Figure 4(c) along with the SEDONA models. Due to less ^{56}Ni in Model 1, the luminosity in the early phase is dimmer than the other models. Increasing ^{56}Ni and distributing to outer layers (~16,000 km s^{−1}) increases the flux in the early times. The effect of ϵ is not seen in the model bolometric light curves. The model parameters are listed in Table 1.

Considering the violent merger density profile, we find that all the models can reproduce the observed light curves and spectra fairly reasonably. Using non-LTE calculations in one dimension, Shen et al. (2021) showed that there is a reduction in Fe II line blanketing and Ca II emission after peak, which increases the magnitude in *U* and *B* bands and decreases in the *I* band, while the *V* band is mostly unaffected. A detailed three-dimensional, non-LTE consideration of the radiation diffusion treating fluorescence for each line separately may give a better match to the observables of SN 2011aa.

6. Discussions

For normal SNe Ia, the average decline rate $\Delta m_{15}(B)$ is 1.2 mag with a peak *B*-band magnitude of -19.3 ± 0.1 mag (Benetti et al. 2005). They show presence of a secondary maximum in *I*-band light curve. The average expansion velocity near maximum is $10,600 \pm 400$ km s^{−1} (Wang et al. 2009b). The favored explosion mechanisms for the normal SNe Ia are the delayed detonation (Mazzali et al. 2007) in an M_{ch} or detonation in a sub- M_{ch} WD (Sim et al. 2010).

SN 2011aa is the slowest declining type Ia SN with a $\Delta m_{15}(B)$ of 0.59 ± 0.07 mag and a peak magnitude of -19.30 ± 0.27 mag. Analytical models indicate ^{56}Ni mass is $0.87 M_\odot$ and ejected mass is between 1.76 and $2.64 M_\odot$. The secondary maximum in the *I* band is as bright as the primary. The Si II velocity evolution shows a plateau after the maximum. The velocity plateau can be explained in terms of a merger scenario where there is a C-O WD inside an extended envelope (Khokhlov et al. 1993). This extended envelope is formed by the destruction of the secondary WD. A detonation shock wave propagating outwards will collide with this low-density envelope and an inward shock wave will cause deceleration of the outward moving material. The duration of

the plateau observed in the velocity will be dependent on the mass of the envelope. Due to the interaction of the shock wave with the envelope, there will be density and pressure gradients that will cause mixing of the materials in the ejecta. The velocity of C II $\lambda 6580$ and C II $\lambda 7234$ is less than the velocity of Si II $\lambda 6355$. This can be due to C II present in the inner layers or the clumping/line-of-sight effect. SN 2011aa shows slow decline similar to that seen in super-Chandra objects; however, the spectral evolution is not similar to either normal or super-Chandra objects. The merger scenario produces similar ^{56}Ni mass as compared to normal SNe Ia and more ejecta mass ($\sim 1.95 M_{\odot}$). So, the peak luminosity is similar to normal SNe Ia and with more ejecta the diffusion time for the photons is large making the decline rate slower. In this work, we have demonstrated that SN 2011aa with a slower decline rate but a normal peak magnitude can be explained by the violent merger of white dwarfs.

We thank the anonymous referee for very useful comments and suggestions. We thank the staff of IAO, Hanle and CREST, Hosakote that made the observations possible. The facilities at IAO and CREST are operated by the Indian Institute of Astrophysics, Bangalore. We also thank the observers of HCT who shared their valuable time for Target of Opportunity (ToO) observations during the initial follow-up. This work has made use of the NASA Astrophysics Data System⁶ (ADS), the NASA/IPAC extragalactic database⁷ (NED NASA/IPAC Extragalactic Database (NED 2019)), and NASA/IPAC Infrared Science Archive⁸ (IRSA IRSA 2022), which is operated by the Jet Propulsion Laboratory, California Institute of Technology. We acknowledge Weizmann Interactive Supernova Data REpository⁹ (WiSeREP; Yaron & Gal-Yam 2012). This research has made use of the data obtained from the High Energy Astrophysics Science Archive Research Center (HEASARC),¹⁰ a facility of the Astrophysics Science Division at NASA/GSFC and of the Smithsonian Astrophysical Observatory's High Energy Astrophysics Division. This work made use of the Heidelberg Supernova Model Archive (HESMA;¹¹ Kromer et al. 2017). This research has made use of the Spanish Virtual Observatory¹² (Rodrigo & Solano 2020). We acknowledge the usage of the HyperLeda database¹³ (Makarov et al. 2014).

The analysis has made use of the following software and packages: (i) *Image Reduction and Analysis Facility* (IRAF), Tody (1993); (ii) PyRAF, Science Software Branch at STScI (2012); (iii) NumPy, Harris et al. (2020); (iv) Matplotlib, Hunter (2007); (v) Scipy, Virtanen et al. (2020); (vi) pandas, pandas development team (2020); (vii) Astropy, Astropy Collaboration et al. (2013); (viii) emcee, Foreman-Mackey et al. (2013); (ix) scikit-learn, Pedregosa et al. (2011); and (x) SEDONA, Kasen et al. (2006).

Data and Model Availability

Reduced spectra presented in this paper will be made available in the WiSeREP archive. Photometric data is given as data behind Figure 1. The reduced spectra in Figure 2 are given as data behind the figure. The parameter and ejecta grid files for the four models generated with SEDONA are provided in the online journal (Table 1).

ORCID iDs

Anirban Dutta  <https://orcid.org/0000-0002-7708-3831>
G. C. Anupama  <https://orcid.org/0000-0003-3533-7183>
D. K. Sahu  <https://orcid.org/0000-0002-6688-0800>

References

- Ashall, C., Lu, J., Hsiao, E. Y., et al. 2021, *ApJ*, **922**, 205
Astropy Collaboration, Robitaille, T. P., Tollerud, E. J., et al. 2013, *A&A*, **558**, A33
Baron, E., Höflich, P., Krisciunas, K., et al. 2012, *ApJ*, **753**, 105
Benetti, S., Cappellaro, E., Mazzali, P. A., et al. 2005, *ApJ*, **623**, 1011
Blanton, M. R., & Roweis, S. 2007, *AJ*, **133**, 734
Branch, D., & Wheeler, J. C. 2017, *Supernova Explosions* (Berlin: Springer), doi:10.1007/978-3-662-55054-0
Branch, D., Dang, L. C., Hall, N., et al. 2006, *PASP*, **118**, 560
Brown, P. J., Holland, S. T., Immler, S., et al. 2009, *AJ*, **137**, 4517
Brown, P. J., Kuin, P., Scalzo, R., et al. 2014, *ApJ*, **787**, 29
Cao, Y., Johansson, J., Nugent, P. E., et al. 2016, *ApJ*, **823**, 147
Cao, Y., Kulkarni, S. R., Howell, D. A., et al. 2015, *Natur*, **521**, 328
Cappellaro, E., Mazzali, P. A., Benetti, S., et al. 1997, *A&A*, **328**, 203
Cardelli, J. A., Clayton, G. C., & Mathis, J. S. 1989, *ApJ*, **345**, 245
Chakradhari, N. K., Sahu, D. K., Srivastav, S., & Anupama, G. C. 2014, *MNRAS*, **443**, 1663
Chatzopoulos, E., Wheeler, J. C., & Vinko, J. 2012, *ApJ*, **746**, 121
Colgate, S. A., & McKee, C. 1969, *ApJ*, **157**, 623
Dilday, B., Howell, D. A., Cenko, S. B., et al. 2012, *Sci*, **337**, 942
Dutta, A., Sahu, D. K., Anupama, G. C., et al. 2022, *ApJ*, **925**, 217
Dutta, A., Singh, A., Anupama, G. C., Sahu, D. K., & Kumar, B. 2021, *MNRAS*, **503**, 896
Filippenko, A. V., Richmond, M. W., Branch, D., et al. 1992, *AJ*, **104**, 1543
Fink, M., Kromer, M., Hillebrandt, W., et al. 2018, *A&A*, **618**, A124
Foreman-Mackey, D., Hogg, D. W., Lang, D., & Goodman, J. 2013, *PASP*, **125**, 306
Friedman, A. S., Wood-Vasey, W. M., Marion, G. H., et al. 2015, *ApJS*, **220**, 9
Graham, M. L., Harris, C. E., Fox, O. D., et al. 2017, *ApJ*, **843**, 102
Gurugubelli, K., Sahu, D. K., Anupama, G. C., Anto, P., & Arora, S. 2011, *CBET*, **2653**, 3
Harris, C. R., Millman, K. J., van der Walt, S. J., et al. 2020, *Natur*, **585**, 357
Hicken, M., Garnavich, P. M., Prieto, J. L., et al. 2007, *ApJL*, **669**, L17
Höflich, P., Khokhlov, A., Wheeler, J. C., et al. 1996, *ApJL*, **472**, L81
Howell, D. A., Sullivan, M., Nugent, P. E., et al. 2006, *Natur*, **443**, 308
Hoyle, F., & Fowler, W. A. 1960, *ApJ*, **132**, 565
Hunter, J. D. 2007, *CSE*, **9**, 90
IRSA 2022, Galactic Dust Reddening and Extinction Service, Accessed on 2022/03/10, IPAC, doi:10.26131/IRSA537
Jha, S. W., Maguire, K., & Sullivan, M. 2019, *NatAs*, **3**, 706
Kasen, D., Thomas, R. C., & Nugent, P. 2006, *ApJ*, **651**, 366
Khatami, D. K., & Kasen, D. N. 2019, *ApJ*, **878**, 56
Khokhlov, A., Mueller, E., & Höflich, P. 1993, *A&A*, **270**, 223
Krisciunas, K., Li, W., Matheson, T., et al. 2011, *AJ*, **142**, 74
Kromer, M., Ohlmann, S., & Röpke, F. K. 2017, *Mem. Soc. Astron. Italiana*, **88**, 312
Kromer, M., Pakmor, R., Taubenberger, S., et al. 2013, *ApJL*, **778**, L18
Kushnir, D., & Katz, B. 2019, *RNAAS*, **3**, 162
Kushnir, D., Katz, B., Dong, S., Livne, E., & Fernández, R. 2013, *ApJL*, **778**, L37
Langer, N., Deutschmann, A., Wellstein, S., & Höflich, P. 2000, *A&A*, **362**, 1046
Li, W., Bloom, J. S., Podsiadlowski, P., et al. 2011, *Natur*, **480**, 348
Li, W., Filippenko, A. V., Chornock, R., et al. 2003, *PASP*, **115**, 453
Liu, W. M., Chen, W. C., Wang, B., & Han, Z. W. 2010, *A&A*, **523**, A3
Lu, J., Ashall, C., Hsiao, E. Y., et al. 2021, *ApJ*, **920**, 107
Maeda, K., & Terada, Y. 2016, *IJMPD*, **25**, 1630024

⁶ <https://ui.adsabs.harvard.edu/>

⁷ <https://ned.ipac.caltech.edu/>

⁸ <https://irsa.ipac.caltech.edu/applications/DUST/>

⁹ <https://wiserep.weizmann.ac.il/>

¹⁰ <https://heasarc.gsfc.nasa.gov>

¹¹ <https://hesma.h-its.org>

¹² <https://svo.cab.inta-csic.es>

¹³ <http://leda.univ-lyon1.fr>

- Magee, M. R., & Maguire, K. 2020, *A&A*, **642**, A189
- Makarov, D., Prugniel, P., Terekhova, N., Courtois, H., & Vauglin, I. 2014, *A&A*, **570**, A13
- Mazzali, P. A., Röpke, F. K., Benetti, S., & Hillebrandt, W. 2007, *Sci*, **315**, 825
- Munari, U., & Renzini, A. 1992, *ApJL*, **397**, L87
- NASA/IPAC Extragalactic Database (NED) 2019, NASA/IPAC Extragalactic Database (NED), Accessed on 2022/03/10, IPAC, doi:10.26132/NED1
- Nugent, P. E., Sullivan, M., Cenko, S. B., et al. 2011, *Natur*, **480**, 344
- Pakmor, R., Kromer, M., Röpke, F. K., et al. 2010, *Natur*, **463**, 61
- Pakmor, R., Kromer, M., Taubenberger, S., et al. 2012, *ApJL*, **747**, L10
- pandas development team 2020, pandas-dev/pandas: Pandas, latest, Zenodo, doi:10.5281/zenodo.3509134
- Pankey, T. J. 1962, PhD thesis, Howard Univ. Washington, DC
- Parrent, J. T., Thomas, R. C., Fesen, R. A., et al. 2011, *ApJ*, **732**, 30
- Pedregosa, F., Varoquaux, G., Gramfort, A., et al. 2011, *J. Mach. Learn. Res.*, **12**, 2825
- Phillips, M. M. 1993, *ApJL*, **413**, L105
- Poole, T. S., Breeveld, A. A., Page, M. J., et al. 2008, *MNRAS*, **383**, 627
- Puckett, T., Newton, J., Balam, D. D., et al. 2011, *CBET*, **2653**, 1
- Raskin, C., & Kasen, D. 2013, *ApJ*, **772**, 1
- Raskin, C., Timmes, F. X., Scannapieco, E., Diehl, S., & Fryer, C. 2009, *MNRAS*, **399**, L156
- Rasmussen, C., & Williams, C. 2006, *Gaussian Processes for Machine Learning, Adaptive Computation and Machine Learning*, 248 (Cambridge, MA: MIT Press)
- Rodrigo, C., & Solano, E. 2020, in XIV.0 Scientific Meeting (virtual) of the Spanish Astronomical Society 182 (Barcelona: Spanish Astronomical Society)
- Rosswog, S., Kasen, D., Guillochon, J., & Ramirez-Ruiz, E. 2009, *ApJL*, **705**, L128
- Schlafly, E. F., & Finkbeiner, D. P. 2011, *ApJ*, **737**, 103
- Science Software Branch at STScI 2012, PyRAF: Python alternative for IRAF, Astrophysics Source Code Library, ascl:1207.011
- Shen, K. J., Blondin, S., Kasen, D., et al. 2021, *ApJL*, **909**, L18
- Silverman, J. M., Nugent, P. E., Gal-Yam, A., et al. 2013, *ApJ*, **772**, 125
- Sim, S. A., Röpke, F. K., Hillebrandt, W., et al. 2010, *ApJL*, **714**, L52
- Stritzinger, M., Mazzali, P. A., Sollerman, J., & Benetti, S. 2006, *A&A*, **460**, 793
- Taubenberger, S. 2017, in *Handbook of Supernovae*, ed. A. W. Alsabti & P. Murdin (Berlin: Springer), 317
- Taubenberger, S., Benetti, S., Childress, M., et al. 2011, *MNRAS*, **412**, 2735
- Taubenberger, S., Kromer, M., Pakmor, R., et al. 2013, *ApJL*, **775**, L43
- Tody, D. 1993, in *ASP Conf. Ser. 52, Astronomical Data Analysis Software and Systems II*, ed. R. J. Hanisch, R. J. V. Brissenden, & J. Barnes (San Francisco, CA: ASP), 173
- Turatto, M., Benetti, S., & Cappellaro, E. 2003, in *From Twilight to Highlight: The Physics of Supernovae*, ed. W. Hillebrandt & B. Leibundgut (Berlin: Springer), 200
- van den Heuvel, E. P. J., Bhattacharya, D., Nomoto, K., & Rappaport, S. A. 1992, *A&A*, **262**, 97
- Virtanen, P., Gommers, R., Oliphant, T. E., et al. 2020, *NatMe*, **17**, 261
- Wang, X., Filippenko, A. V., Ganeshalingam, M., et al. 2009b, *ApJL*, **699**, L139
- Wang, X., Li, W., Filippenko, A. V., et al. 2009a, *ApJ*, **697**, 380
- Yaron, O., & Gal-Yam, A. 2012, *PASP*, **124**, 668
- Yoon, S. C., & Langer, N. 2005, *A&A*, **435**, 967